Otoyama *et al. Energy Mater.* **2025**, *5*, 500126
DOI: 10.20517/energymater.2025.44

Energy Materials

Article

Open Access

Check for updates

Li_xVS_y nanocomposite electrodes for high-energy carbon-additive-free all-solid-state lithium-sulfur batteries

Misae Otoyama[1,*], Mizue Wanibuchi[2], Tomonari Takeuchi[1], Naoya Ishida[1], Noboru Taguchi[1], Mitsunori Kitta[1], Hikaru Sano[2], Koji Kawamoto[2], Toyoki Okumura[1], Kentaro Kuratani[1], Hikari Sakaebe[1,3,*]

[1]Research Institute of Electrochemical Energy, National Institute of Advanced Industrial Science and Technology (AIST), Ikeda, Osaka 563-8577, Japan.
[2]Consortium for Lithium Ion Battery Technology and Evaluation Research Center (LIBTEC), Ikeda, Osaka 563-8577, Japan.
[3]Institute for Materials Chemistry and Engineering, Kyushu University, Kasuga, Fukuoka 816-8580, Japan.

***Correspondence to:** Dr. Misae Otoyama, Research Institute of Electrochemical Energy, National Institute of Advanced Industrial Science and Technology (AIST), 1-8-31 Midorigaoka, Ikeda, Osaka 563-8577, Japan. E-mail: misae-otoyama@aist.go.jp; Dr. Hikari Sakaebe, Research Institute of Electrochemical Energy, National Institute of Advanced Industrial Science and Technology (AIST), 1-8-31 Midorigaoka, Ikeda, Osaka 563-8577, Japan. E-mail: sakaebe@cm.kyushu-u.ac.jp

How to cite this article: Otoyama, M.; Wanibuchi, M.; Takeuchi, T.; Ishida, N.; Taguchi, N.; Kitta, M.; Sano, H.; Kawamoto, K.; Okumura, T.; Kuratani, K.; Sakaebe, H. LixVSy nanocomposite electrodes for high-energy carbon-additive-free all-solid-state lithium-sulfur batteries. *Energy Mater.* **2025**, *5*, 500126. https://dx.doi.org/10.20517/energymater.2025.44

Received: 25 Feb 2025 **First Decision:** 1 Apr 2025 **Revised:** 22 Apr 2025 **Accepted:** 25 Apr 2025 **Published:** 25 Jun 2025

Academic Editors: Meicheng Li, Yoon Hwa **Copy Editor:** Fangling Lan **Production Editor:** Fangling Lan

Abstract

All-solid-state (ASS) lithium-sulfur batteries are promising power sources with the potential for high capacity and safety. Lithium metal polysulfide cathodes can address issues arising from the low electronic conductivity of Li_2S and S. This study synthesized lithium vanadium polysulfides (Li_xVS_y) by the mechanochemical treatment of Li_2S and V_2S_3. The Li_xVS_y system contains nanocomposites of Li_2S and $LiVS_2$ in an amorphous matrix; lithiation and delithiation occur in both Li_2S and $LiVS_2$ during charging and discharging. $LiVS_2$ enhances the electronic conductivity of Li_xVS_y (~10^{-1}-10^{-2} S cm^{-1}) and the reversibility of charge-discharge reactions because of its high electronic conductivity and layered structure. Therefore, ASS batteries with Li_xVS_y show high capacity (~650 mAh g^{-1}), even without conductive additives. Here, ASS full cells with high loading assembled using a composite cathode comprising $Li_8VS_{5.5}$ and a solid electrolyte in a 80:20 (wt.%) ratio (33 mg cm^{-2}) and a composite Si anode (10.4 mg cm^{-2}) exhibited a high areal capacity of 15 mAh cm^{-2}, resulting in calculation of high energy densities of 853 Wh L^{-1} and 515 Wh kg^{-1} when assuming the cells were enlarged and stacked. This study is expected to expedite research on the development of high-performance ASS batteries.

Keywords: Lithium-vanadium polysulfide cathodes, all-solid-state lithium-sulfur batteries, sulfide solid electrolytes, high energy density, nanocomposites

INTRODUCTION

Lithium-sulfur batteries have attracted considerable attention as promising next-generation batteries owing to their high capacity and low cost[1,2]. All-solid-state (ASS) lithium-sulfur batteries containing sulfide solid electrolytes (SEs) are particularly promising for practical use because of several reasons. First, there is no risk of polysulfide dissolution in such systems; in contrast, conventional lithium batteries with organic liquid electrolytes undergo capacity degradation due to the formation and dissolution of polysulfides in the electrolyte[3,4]. Second, compared with systems containing oxide-based cathodes, such as $LiCoO_2$ and $LiNi_xMn_yCo_zO_2$, facile solid-solid interface formation is observed in lithium-sulfur batteries containing sulfide SEs, resulting in sufficient contact between the cathode and sulfide SE through pressing[5,6]. Third, sulfide SEs exhibiting high ionic conductivities of ~10^{-2}-10^{-3} S cm^{-1} have been developed[7-10]. However, because of the low electronic conductivities of Li_2S and S, sulfur-based cathodes typically require 10-20 wt.% of composite cathodes[11]. In addition, carbon additives degrade the cycle performance of sulfide ASS batteries (ASSBs) by promoting the electrochemical decomposition of sulfide SEs[12-15]. Therefore, cathodes with high electronic conductivities should be developed to fabricate ASSBs that exhibit a long cycle life, even without carbon additives.

Some metal polysulfides and composite electrodes do not require carbon because of their high electronic conductivity[16-18]. In addition, Li-containing metal polysulfide cathodes can employ various anodes, such as Si and Si-based alloys, besides lithium metal. Li_3NbS_4[18] and Li_3CuS_2[19] show electronic conductivities of 2×10^{-3} and 9.5×10^{-3} S cm^{-1}, respectively, and ASSBs containing these electrodes show reversible capacities of 386 and 380 mAh g^{-1}, respectively, without any conductive additives. Our group has focused on lithium vanadium polysulfides, Li_xVS_y[20], because vanadium sulfides show higher electronic conductivity[21-25]. Our previous publication reports that Li_xVS_y (x = 5-9, y = 4-6) shows a high electronic conductivity of ~10^{-1}-10^{-2} S cm^{-1}[20]. Moreover, an ASSB with a composite electrode containing Li_5VS_4 and the SE in an 80:20 ratio (wt.%) shows 94% of the theoretical capacity (626 mAh g^{-1}) without any conductive additives[20]. Recently, some lithium-containing vanadium sulfides, such as $90(0.75Li_2S{\cdot}0.25V_2S_3){\cdot}10LiI$[24] and core-shell $Li_2S/LiVS_2$[25], have been reported as high-capacity cathodes. $90(0.75Li_2S{\cdot}0.25V_2S_3){\cdot}10LiI$ systems comprise $LiVS_2$ and Li_2S-LiI nanoparticles dispersed in an Li_2S-V_2S_3-LiI amorphous matrix, resulting in electrode-electrolyte bifunctional features[24]. In contrast, core-shell $Li_2S/LiVS_2$ systems comprise a Li_2S core and a $LiVS_2$ shell, and Li_xVS_2 functions as an interfacial redox mediator in such systems[25]. X-ray diffraction (XRD) measurements indicate that Li_xVS_y is composed of Li_2S and $LiVS_2$[20]. However, the underlying reason for the high capacity of such systems, based on the detailed structure of Li_xVS_y, has not been systematically investigated to date.

In this study, the detailed structural analysis of Li_xVS_y, including its charged and discharged states, was conducted using synchrotron XRD measurements, transmission electron microscopy (TEM), and X-ray absorption fine structure (XAFS) measurements to understand the reaction mechanism of systems comprising Li_xVS_y. High-loading full cells comprising $Li_8VS_{5.5}$ and Si without any conductive additives showed a high areal capacity of 15 mAh cm^{-2}. According to the calculation, a high energy density exceeding 800 Wh L^{-1} and 500 Wh kg^{-1} will be achieved on enlargement and stacking of the full cells.

EXPERIMENTAL

Preparation of Li_xVS_y cathodes

Li_xVS_y (x = 5-9, y = 4-6) cathodes were prepared by the mechanochemical treatment of Li_2S (99%, Kojundo Chemical Lab. Co. Ltd.) and V_2S_3 (99%; Kojundo Chemical Lab. Co. Ltd.) according to a previously

described method[20]. A high-crystallinity sample of $Li_8VS_{5.5}$ (denoted as $Li_8VS_{5.5}$-HC) was synthesized under modified processing conditions. Stoichiometric mixtures of Li_2S and V_2S_3 were weighed - 6 g for $Li_8VS_{5.5}$-HC and 1 g for standard $Li_8VS_{5.5}$ - and placed into ZrO_2 milling pots (250 mL for $Li_8VS_{5.5}$-HC and 45 mL for $Li_8VS_{5.5}$) each loaded with ZrO_2 balls (30 balls of 15 mm diameter for $Li_8VS_{5.5}$-HC and 15 balls of 10 mm diameter for $Li_8VS_{5.5}$). All procedures were conducted under a dry Ar atmosphere. Mechanical milling was performed using planetary ball mills: a Pulverisette 5 classic line (Fritsch) for $Li_8VS_{5.5}$-HC and a Pulverisette 7 premium line (Fritsch) for $Li_8VS_{5.5}$. Both mixtures were milled for 160 h at rotational speeds of 300 rpm for $Li_8VS_{5.5}$-HC and 400 rpm for $Li_8VS_{5.5}$.

Construction of ASSBs

Composite cathodes were prepared by gently mixing Li_xVS_y and argyrodite-type sulfide SEs (Mitsui Mining & Smelting Co., Ltd.) for 1 h using a planetary ball mill (Pulverisette 7 premium line, Fritsch). To assemble ASS half-cells with a diameter of 10 mm, the sulfide SE was pressed at 30 MPa to fabricate an SE layer, and the composite cathode (10 mg) was placed on the SE layer and pressed at 720 MPa; subsequently, the Li-In alloy was attached to the other side of the SE layer. The resultant cell was sandwiched between two stainless steel (SUS) rods used as current collectors and confined at 160 MPa. Each 1-centimeter square ASS full cell was constructed using a $Li_8VS_{5.5}$ composite cathode and a composite Si anode; the loading mass of the positive and anode layers was 33 and 10.4 mg cm^{-2}, respectively. The fabricated cells were charged and discharged using a charge-discharge measuring device (TOSCAT-3100, Toyo System Co. Ltd.).

Electronic and ionic conductivity measurements

This study measured the electronic and ionic conductivity of composite cathodes by direct current (DC) polarization tests at 25, 45, and 60 °C. SUS/composite cathode/SUS and SUS/Li-In/SE/composite cathode/SE/Li-In/SUS systems were used for electronic and ionic conductivity measurements, respectively. The loading mass of the composite cathode layer in each system was > 30 mg cm^{-2}.

Synchrotron XRD measurements

Synchrotron XRD was used to analyze pristine Li_xVS_y and composite cathodes in charge and discharge states at the BL19B2 beamline of SPring-8 at room temperature. The samples were sealed in glass capillaries (~0.3 mm diameter) under dry Ar. The wavelength of the synchrotron X-ray was 0.5002 Å calibrated by CeO_2. The RIETAN-FP program was used for Rietveld refinement[26], and multiphases were added one by one while peak identification was carefully performed to sufficiently reduce residual peaks.

Elemental analysis of Li_xVS_y

To investigate the amounts of Li and V in Li_xVS_y, inductively coupled plasma atomic emission spectroscopy (ICP-AES) was conducted using an inductively coupled plasma atomic emission spectrometer (Agilent 5110 VDV, Agilent Technologies, Inc.). Before measurements, the samples were thermally decomposed using acids, and their final volume was adjusted using ultrapure water. The amount of S in the samples was measured using an automatic combustion halogen and sulfur analysis system (HSU-35/SQ-10, Anatec Yanaco Co. Ltd. and ICS-2100, Dionex Corp.).

XAFS measurements

The valence states and local structures of the S and V atoms in Li_xVS_y and composite cathodes after charge and discharge tests were examined by S and V K-edge XAFS measurements at the Synchrotron Radiation Center, Ritsumeikan University. The S and V K-edge spectra of the samples were recorded at the BL-10 and BL-3 beamlines, respectively[27]. The incident X-ray beam was monochromatized with a Ge(111) crystal (2d = 6.532 Å) for S K-edge measurements by the total electron yield method. The photon energy was calibrated with the strong resonance of K_2SO_4 (S 1s → t_2) at 2481.7 eV[28]. For V K-edge measurements in the

conventional transmission mode, the incident X-ray beam was monochromatized with a Si(220) crystal ($2d$ = 3.840 Å). All samples for S and Fe K-edge measurements were sealed in Ar-filled transfer vessels[27] and Al-laminated bags, respectively.

TEM observations

The Li_xVS_y samples were analyzed by a high-resolution transmission electron microscope (Talos F200X, Thermo Fisher Scientific, Inc.). Bright-field TEM micrographs were acquired by a slow-scan charge-coupled device camera (Ceta, FEI Company) at 200 kV of accelerated voltage with 0.5 s exposure time.

Additionally, the composite cathodes before charging and after the second discharging process were analyzed using cryo-scanning TEM (cryo-STEM) on an atomic-resolution analytical electron microscope (JEM-ARM200F, JEOL Ltd.). Before STEM analysis, the samples were thinned to the desired shape using a focused ion beam milling apparatus (NanoDUE' T NB5000, Hitachi High-Tech Corp.). To investigate the elemental mappings in the samples, STEM-energy dispersive X-ray spectroscopy (STEM-EDX) and STEM-electron energy loss spectroscopy (STEM-EELS) were conducted with EDX (JED-2300T, JEOL Ltd.) and EELS (GIF Quantum-ER, Gatan, Inc.) instruments.

RESULTS AND DISCUSSION

Characterization of Li_xVS_y cathodes

Cathode materials with compositions Li_5VS_4, $Li_6VS_{4.5}$, Li_7VS_5, $Li_8VS_{5.5}$, and Li_9VS_6 were synthesized via ball milling of Li_2S and V_2S_3. As reported in our previous study[20], the theoretical capacity of Li_xVS_y compounds increases with higher Li and S content (increasing x and y), whereas the electronic conductivity correspondingly decreases. The initial charge-discharge profiles of half-cells incorporating Li_xVS_y (x = 5-9, y = 4-6) cathodes were also investigated in that study[20]. Among the compositions evaluated, $Li_8VS_{5.5}$ exhibited the highest initial discharge capacity, making it the most promising candidate. Therefore, $Li_8VS_{5.5}$ was selected for further investigation in the present study. Figure 1A and Supplementary Table 1 show the synchrotron XRD patterns and crystallographic data, respectively, of $Li_8VS_{5.5}$. The results of the other Li_xVS_y samples are shown in Supplementary Figure 1 and Supplementary Table 1. The synchrotron XRD patterns of all samples contain diffraction peaks corresponding to Li_2S (space group: $Fm\bar{3}m$) and $LiVS_2$ (space group: $P\bar{3}m1$), indicating the formation of $LiVS_2$ by the reaction of Li_2S and V_2S_3. The molar ratio of all samples from Li_2S to $LiVS_2$ was calculated from their synchrotron XRD patterns [Supplementary Table 1]. Except for Li_5VS_4, the molar and nominal ratios of all samples are similar. The spectrum of Li_5VS_4 contains diffraction peaks corresponding to V_2O_3; notably, the starting material V_2S_3 contains V_2O_3 as an impurity. Li_5VS_4, which requires the highest amount of V_2S_3 among all the Li_xVS_y samples, contained the highest amount of V_2O_3. For Li_5VS_4, the addition of vanadium atoms from V_2O_3 to the mol% of $LiVS_2$ results in $Li_2S/LiVS_2$ (V_2O_3) = 69.1/30.5, which is approximately the same as the nominal ratio of the system. The amounts of Li, V, and S in Li_xVS_y were determined using ICP-AES and an automatic combustion halogen and sulfur analysis system [Supplementary Table 2]. The measurement data for all samples were consistent with their nominal ratios, indicating that S volatilization did not occur during synthesis by ball milling.

Figure 1B and C show the S and V K-edge X-ray absorption near-edge structure (XANES) spectra of the Li_xVS_y samples. The V K-edge spectrum of Li_9VS_6 is not shown in Figure 1C because of its low S/N ratio. In the S K-edge spectra, the peak intensities of Li_2S and $LiVS_2$ increase and decrease, respectively, with increasing x in Li_xVS_y, consistent with the results of synchrotron XRD. Moreover, the V K-edge spectra indicate that the electronic states of V in all the samples are almost the same as those in $LiVS_2$.

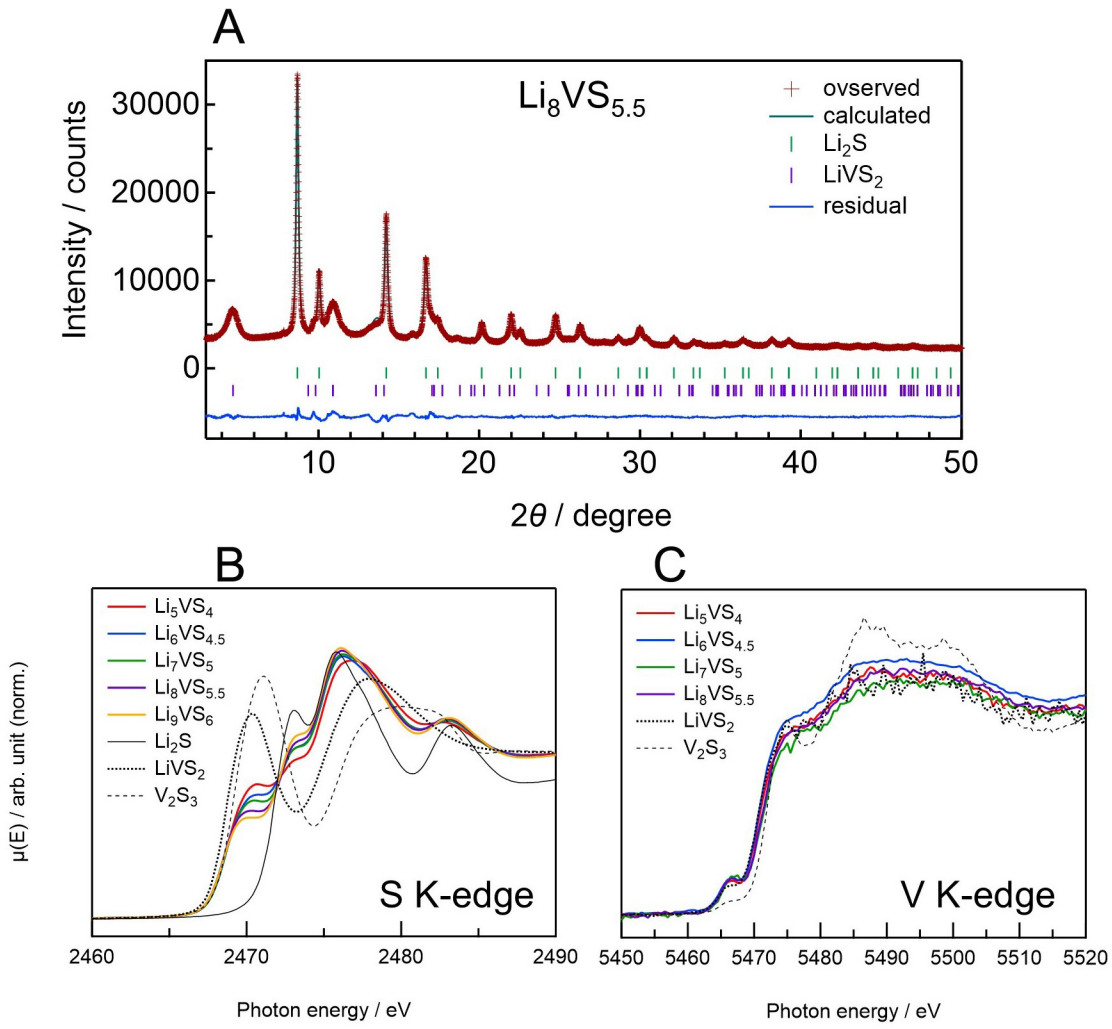

Figure 1. (A) Rietveld analysis of the synchrotron XRD pattern of $Li_8VS_{5.5}$ with R_{wp} = 3.13%, R_e = 1.64%, and S = 1.91. (B) S K-edge and (C) V K-edge XANES spectra of Li_5VS_4, $Li_6VS_{4.5}$, Li_7VS_5, $Li_8VS_{5.5}$, and Li_9VS_6 with reference spectra of Li_2S, $LiVS_2$, and V_2S_3. The V K-edge XANES spectrum of Li_9VS_6 is not shown because of its low S/N ratio.

TEM was used to investigate the microstructures of Li_5VS_4, $Li_6VS_{4.5}$, Li_7VS_5, and $Li_8VS_{5.5}$ [Supplementary Figure 2]. The results indicate that most samples are in an amorphous state. In the TEM image of $Li_8VS_{5.5}$, $LiVS_2$ and Li_2S are mapped in red and green at each lattice spacing [Figure 2A]. The TEM image of $Li_8VS_{5.5}$ shows nanocomposites of Li_2S and $LiVS_2$ distributed in $Li_8VS_{5.5}$. Li_xVS_y cathodes show high electronic conductivity (~10^{-1}-10^{-2} S cm^{-1}) because they comprise highly composited $LiVS_2$ with high electronic conductivity and insulating Li_2S. To compare the mixed states of Li_2S and $LiVS_2$, a $Li_8VS_{5.5}$ sample with high crystallinity (labeled $Li_8VS_{5.5}$-HC) was synthesized under different ball-milling conditions with relatively low mechanical energy. The TEM image of $Li_8VS_{5.5}$-HC [Figure 2B] indicates a higher crystallinity of Li_2S and $LiVS_2$ than that in $Li_8VS_{5.5}$. A comparison of Figure 2A and B indicates that Li_2S and $LiVS_2$ with a large crystallite size exist in $Li_8VS_{5.5}$-HC; in contrast, Li_2S and $LiVS_2$ with a smaller crystallite size are highly mixed in $Li_8VS_{5.5}$. Moreover, $Li_8VS_{5.5}$-HC exhibits a higher electronic conductivity (0.19 S cm^{-1}) than $Li_8VS_{5.5}$ (0.059 S cm^{-1}), possibly because $Li_8VS_{5.5}$-HC contains high-crystallinity $LiVS_2$ with high electronic conductivity. Figure 2C shows the initial charge-discharge curves of ASSBs containing $Li_8VS_{5.5}$ samples. Cells with $Li_8VS_{5.5}$-HC show large hysteresis and low capacity. Moreover, the mixture of Li_2S and $LiVS_2$

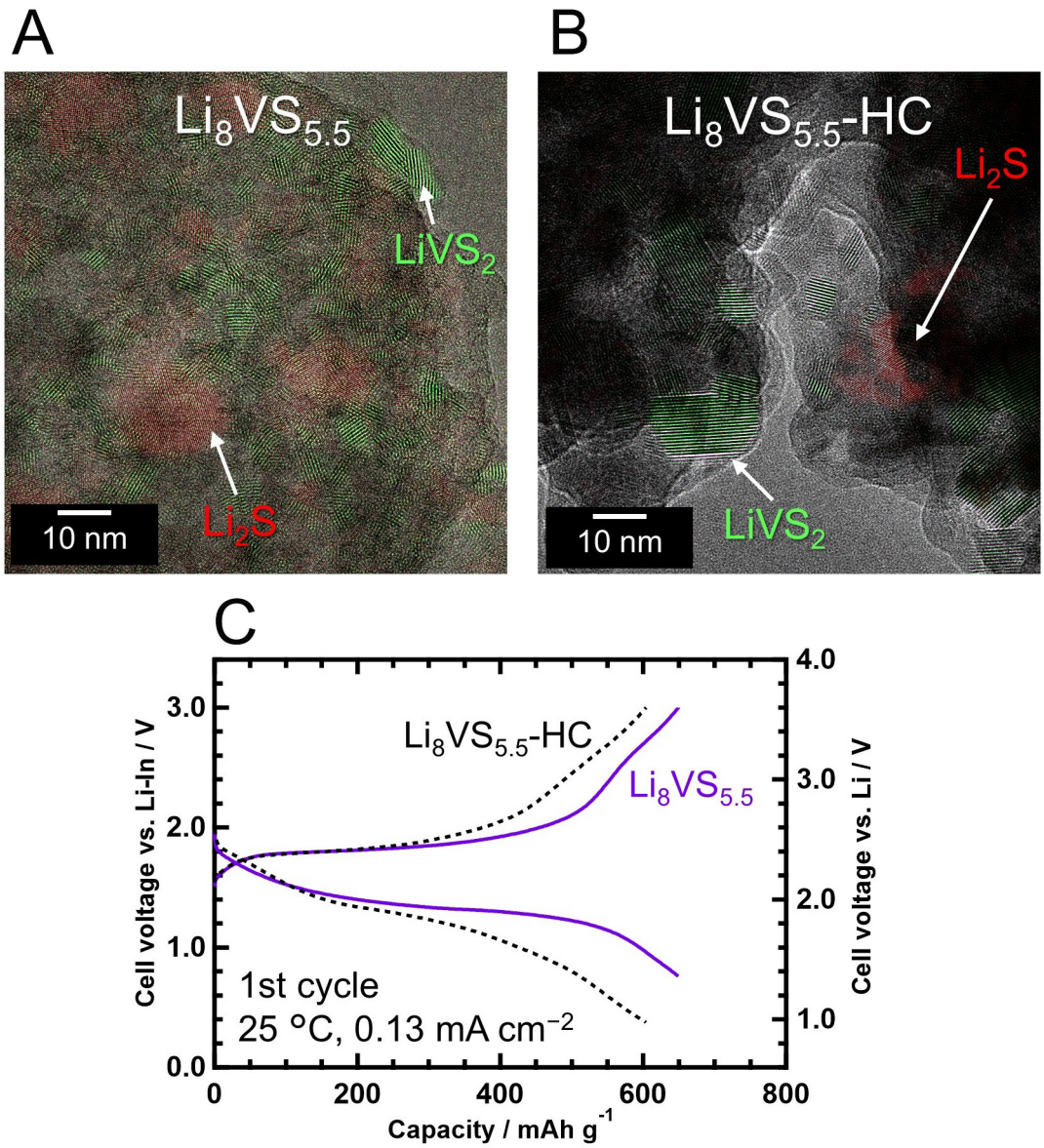

Figure 2. High-resolution TEM images of (A) $Li_8VS_{5.5}$ and (B) $Li_8VS_{5.5}$-HC (high crystallinity) with $LiVS_2$ and Li_2S mapped in red and green, respectively. The color mapping is defined by a difference in lattice spacing. (C) Initial charge-discharge curves of ASSBs containing $Li_8VS_{5.5}$ and $Li_8VS_{5.5}$-HC under a current density of 0.13 mA cm^{-2} at 25 °C.

prepared by hand mixing did not operate in ASSBs. A comparison of $Li_8VS_{5.5}$ samples suggests that high electronic conductivity and a well-dispersed nanocomposite structure comprising Li_2S, which contributes to high capacity, and $LiVS_2$, which provides high electronic conductivity, is essential for optimal performance. As demonstrated in our previous study[20], $Li_8VS_{5.5}$ exhibited the highest initial charge capacity among the Li_xVS_y series (x = 5-9, y = 4-6), indicating that its specific molar ratio of Li_2S to $LiVS_2$ is particularly favorable. Additionally, the presence of amorphous regions within the Li_xVS_y matrix is believed to facilitate efficient pathways for both electronic and ionic transport[24].

Electrochemical properties of $Li_8VS_{5.5}$ cathodes

To determine an optimal composition for electrode fabrication, composite cathodes were prepared by mixing $Li_8VS_{5.5}$ with a sulfide SE at various weight ratios (70/30, 75/25, 80/20, and 85/15). The electronic and ionic conductivities and electrochemical capacities of these composites were systematically analyzed and compared. In our previous study[20], the electronic and ionic conductivities of pure $Li_8VS_{5.5}$ were reported to be 5.9×10^{-2} and 5.6×10^{-6} S cm^{-2} at room temperature, respectively.

Figure 3A shows the electronic conductivities of the fabricated composite cathodes measured by DC polarization at 25 °C. The electronic conductivity is enhanced by increasing the weight ratio of $Li_8VS_{5.5}$. The electronic conductivity of electrodes containing 70 wt.% of $Li_8VS_{5.5}$ is higher than the ionic conductivity of the SE (*ca.* 2×10^{-3} S cm^{-1}); therefore, the $Li_8VS_{5.5}$ composite cathodes exhibit sufficient electronic conductivity. The ionic conductivity values for each composite electrode measured by DC polarization at 25, 45, and 60 °C are shown in Figure 3B. The ionic conductivities of the composite electrodes decrease with increasing content of $Li_8VS_{5.5}$. Notably, the ionic conductivities of the composite electrodes are lower than their electronic conductivities, even at 60 °C, indicating that ionic conduction is a rate-limiting process in the composite electrodes.

Figure 3C shows the discharge capacities of cells containing composite cathodes with various weight ratios of $Li_8VS_{5.5}$ and the SE at 60 °C. Each composite cathode was fabricated with the same amount of $Li_8VS_{5.5}$, and the discharge capacities of the fabricated cells were calculated using the amount of composite cathode. The ionic conductivity of the cells decreases with increasing weight ratio of $Li_8VS_{5.5}$. Moreover, the amount of composite cathode increases, and the electronic conductivity decreases with decreasing weight ratio of $Li_8VS_{5.5}$. The cell with a $Li_8VS_{5.5}$ to SE weight ratio of 80/20 shows the highest discharge capacity owing to an optimal balance of ionic and electronic conductivities.

Figure 3D shows the charge-discharge curves of ASS full cell with $Li_8VS_{5.5}$ and Si electrodes. The cathode contains 33 mg cm^{-2} of the composite cathode consisting of $Li_8VS_{5.5}$ and SE in a weight ratio of 80/20, whereas the anode contains 10.4 mg cm^{-2} of the Si composite electrode. The size of the full cell is a 1 × 1 centimeter square. Considering a discharge capacity of *ca.* 15 mAh cm^{-2} and an average operating voltage of 1.646 V, 20 stacked A4 size (210 mm × 297 mm) ASSBs are expected to show high volumetric and gravimetric energy densities of 853 Wh L^{-1} and 515 Wh kg^{-1}, respectively, in a calculation. The cycling performance of the ASS full cell is shown in Supplementary Figure 3A. The capacity retention rate decreases to ~80% after the 10th cycle. Because $Li_8VS_{5.5}$ shows large volume changes during the charge-discharge process, the cell with a high mass loading shows capacity degradation owing to the disconnection of conduction paths between the solid and solid interfaces. Supplementary Figure 3B demonstrates that a half-cell containing $Li_8VS_{5.5}$ with a low mass loading of 6.4 mg cm^{-2} exhibits excellent cycling performance. Supplementary Figure 3C presents the charge-discharge profiles for the first five cycles of the same cell. With increasing cycle numbers, electrode polarization decreased while capacity improved, indicating progressive activation of the electrode. This activation behavior in the initial cycles is consistent with that observed in previously reported ASS lithium-sulfur batteries[29-31].

The volume-change rate of $Li_8VS_{5.5}$ during the charging process was calculated by estimating the molar volumes of $Li_8VS_{5.5}$ and $VS_{5.5}$ listed in Supplementary Table 3. The molar volume of $Li_8VS_{5.5}$ was calculated from its molar mass and measured density value (2.06 g cm^{-3}). The molar volume of $VS_{5.5}$ was calculated from the molar ratio, molar mass, and density values of S and VS_2. After charging, $Li_8VS_{5.5}$ shows a lower shrinking rate (36.5%) than Li_2S (42.1%). Moreover, compared with Li_2S, $Li_8VS_{5.5}$ shows a better electronic conductivity and volume change rate. To improve the cycle performance of ASSBs containing $Li_8VS_{5.5}$, the

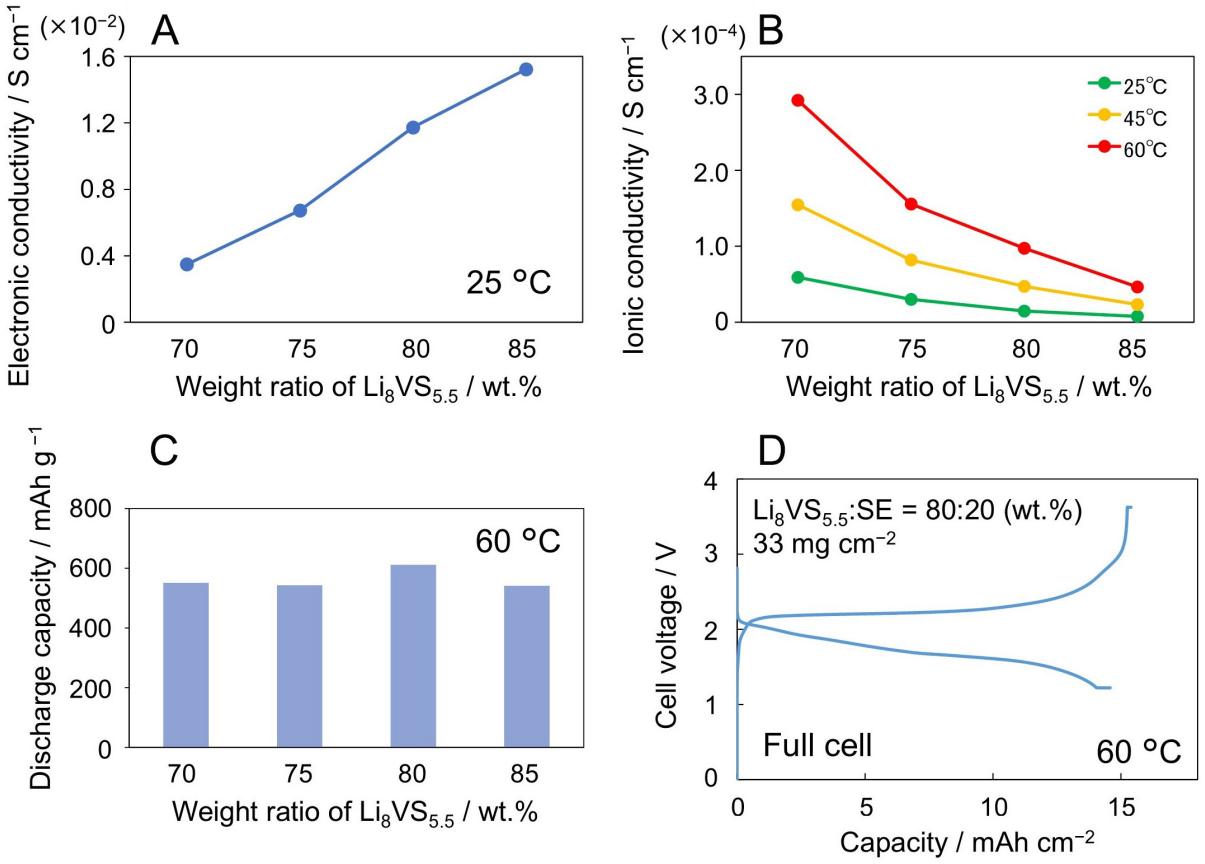

Figure 3. (A) Electronic and (B) ionic conductivities of composite cathodes comprising $Li_8VS_{5.5}$ and the SE in weight ratios of 70/30, 75/25, 80/20, and 85/15. The electronic conductivities are measured at 25 °C, and the ionic conductivities are measured at 25, 45, and 60 °C. (C) Discharge capacities per composite cathode for ASS cells with different weight ratios of $Li_8VS_{5.5}$ and the SE and the same amount of $Li_8VS_{5.5}$. (D) Charge-discharge curves of ASS full cells containing $Li_8VS_{5.5}$ and Si electrodes. The mass loadings of the positive and anodes are 33 and 10.4 mg cm^{-2}, respectively. The cell is charged and discharged with a constant current and voltage at a rate of 0.01 C (until a rate of 0.001 C) over cut-off voltages of 1.22-3.62 V at 60 °C.

volume changes of $Li_8VS_{5.5}$ during charge-discharge tests should be investigated by *operando* measurements. Several approaches have been proposed for reducing crack formation in cells, such as selecting anodes with large volume changes to adjust the total volume change of cells. Details regarding the volume changes of $Li_8VS_{5.5}$ will be discussed in our next paper.

Reaction mechanism of $Li_8VS_{5.5}$ cathodes

$Li_8VS_{5.5}$ enables the construction of high-energy-density ASSBs. To investigate the structural changes during charging and discharging, synchrotron XRD measurements were conducted on composite $Li_8VS_{5.5}$ cathodes before and after charge and discharge [Figure 4]. For the XRD measurements, the ASSBs with a $Li_8VS_{5.5}$ to SE weight ratio of 85/15 were fabricated to detect structural changes of $Li_8VS_{5.5}$ clearly by increasing amount of $Li_8VS_{5.5}$ in composite cathodes. The XRD patterns of $Li_8VS_{5.5}$ and the SE are shown in Figure 4. The XRD pattern before charging [Figure 4A] contains diffraction peaks attributable to Li_2S, $LiVS_2$, and the SE, whereas that after charging [Figure 4B] mainly contains diffraction peaks attributable to the SE, possibly owing to the formation of amorphous S by the delithiation of Li_2S. In addition, the diffraction peaks attributed to $LiVS_2$ are shifted to higher angles because of delithiation from $LiVS_2$. Moreover, the XRD pattern after charging indicates the partial decomposition of the SE to LiCl. The XRD pattern recorded after the discharging process [Figure 4C] contains diffraction peaks attributed to Li_2S resulting from lithiation

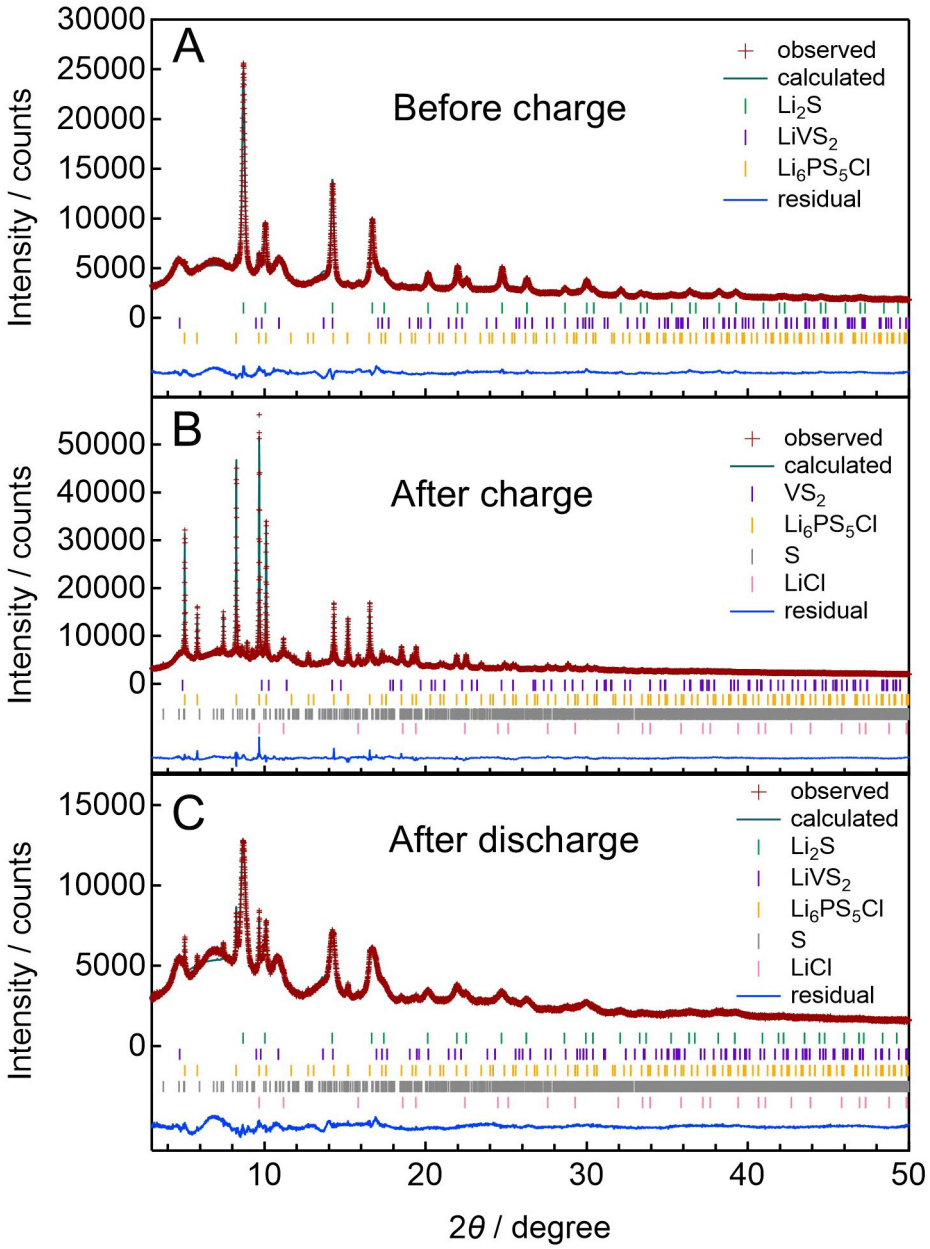

Figure 4. Rietveld analysis of the synchrotron XRD patterns of $Li_8VS_{5.5}$ composite cathodes (A) before charging, (B) after charging, and (C) after discharging.

to S. Furthermore, the diffraction peaks corresponding to $LiVS_2$ shift to lower angles after discharge, suggesting lithiation to form VS_2. Notably, elemental S and LiCl remain in the composite cathodes post-discharge. Modifications such as O-doping have been proposed as effective strategies to mitigate the decomposition of the SE[32]. Table 1 shows the crystallographic data of $LiVS_2$ in the $Li_8VS_{5.5}$ composite cathodes and reference data for $LiVS_2$ and VS_2[33]. The *a* and *c* axes shrink after charging, corresponding to structural changes from $LiVS_2$ to VS_2. After discharging, the *a* and *c* axes change to their pristine states, indicating the reversible formation of $LiVS_2$.

Table 1. Crystallographic data of $LiVS_2$ in $Li_8VS_{5.5}$ composite cathodes (a) before charging, (b) after charging, and (c) after discharging, and reference data of $LiVS_2$ and VS_2

	(a) Before charge	(b) After charge	(c) After discharge	$LiVS_2$ [33]	VS_2 [33]
a/Å	3.374(2)	3.233(5)	3.393(4)	3.381	3.218
c/Å	6.064(3)	5.847(9)	6.055(7)	6.139	5.755

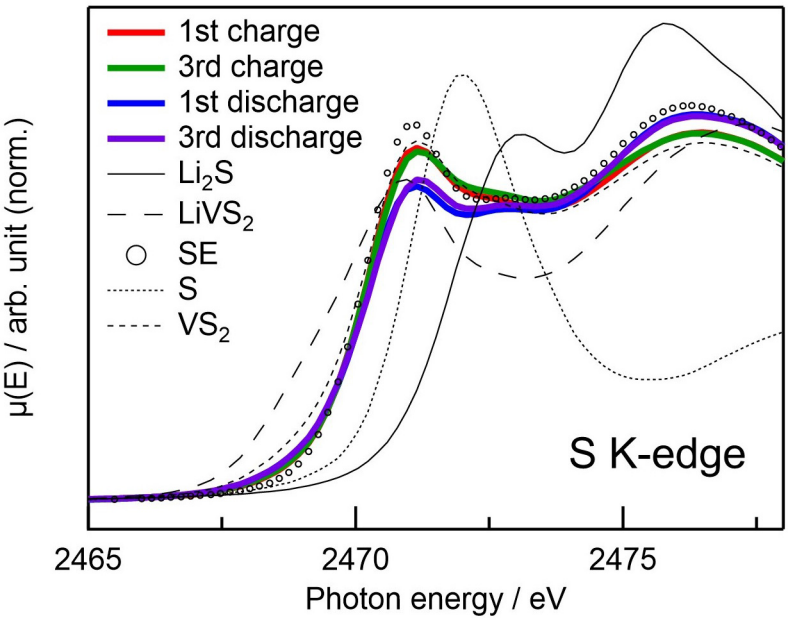

Figure 5. S K-edge XANES spectra of $Li_8VS_{5.5}$ composite cathodes before and after the first and third charge and discharge tests.

Figure 5 shows the S K-edge spectra of the composite cathodes after the first and third charge and discharge. The spectra of the samples after the first charge and discharge are similar to the patterns after the third charge and discharge, respectively, suggesting that the structure changes reversibly over a few cycles.

The XRD patterns and XANES spectra before and after charge-discharge tests indicate reversible delithiation and lithiation. Cryo-STEM measurements were conducted on the $Li_8VS_{5.5}$ composite cathode to investigate nanoscale structural changes after the second discharge test. Figure 6A and Supplementary Figure 4 show the bright-field STEM (BF-STEM) and high-angle annular dark-field STEM (HAADF-STEM) images of the composite electrodes. A red square highlights the EDX measurement area. Figures 6B-G show the annular dark field STEM (ADF-STEM) images and count mappings of the P, Cl, V, S, and O K-edges of the measurement area. In the mapping results of P, Cl, and V, the bright contrast areas highlighted by yellow circles in the ADF-STEM image and the other areas indicate the SE and $Li_8VS_{5.5}$, respectively. Figure 7A-D shows the STEM-EELS mapping results of the measurement area; the yellow circles and other areas in the HAADF-STEM image indicate SE and $Li_8VS_{5.5}$, respectively. The intensity of Li and S in the $Li_8VS_{5.5}$ area decreases toward the interface between $Li_8VS_{5.5}$ and the SE, which is highlighted with orange dotted circles. The thickness of the low-intensity area is ~200 nm. No low-intensity area was observed before the charge-discharge test (not shown here); therefore, the interface was assumed to change during charge-discharge testing. Moreover, Li in the SE area showed low intensity, suggesting that the SE near $Li_8VS_{5.5}$ was delithiated.

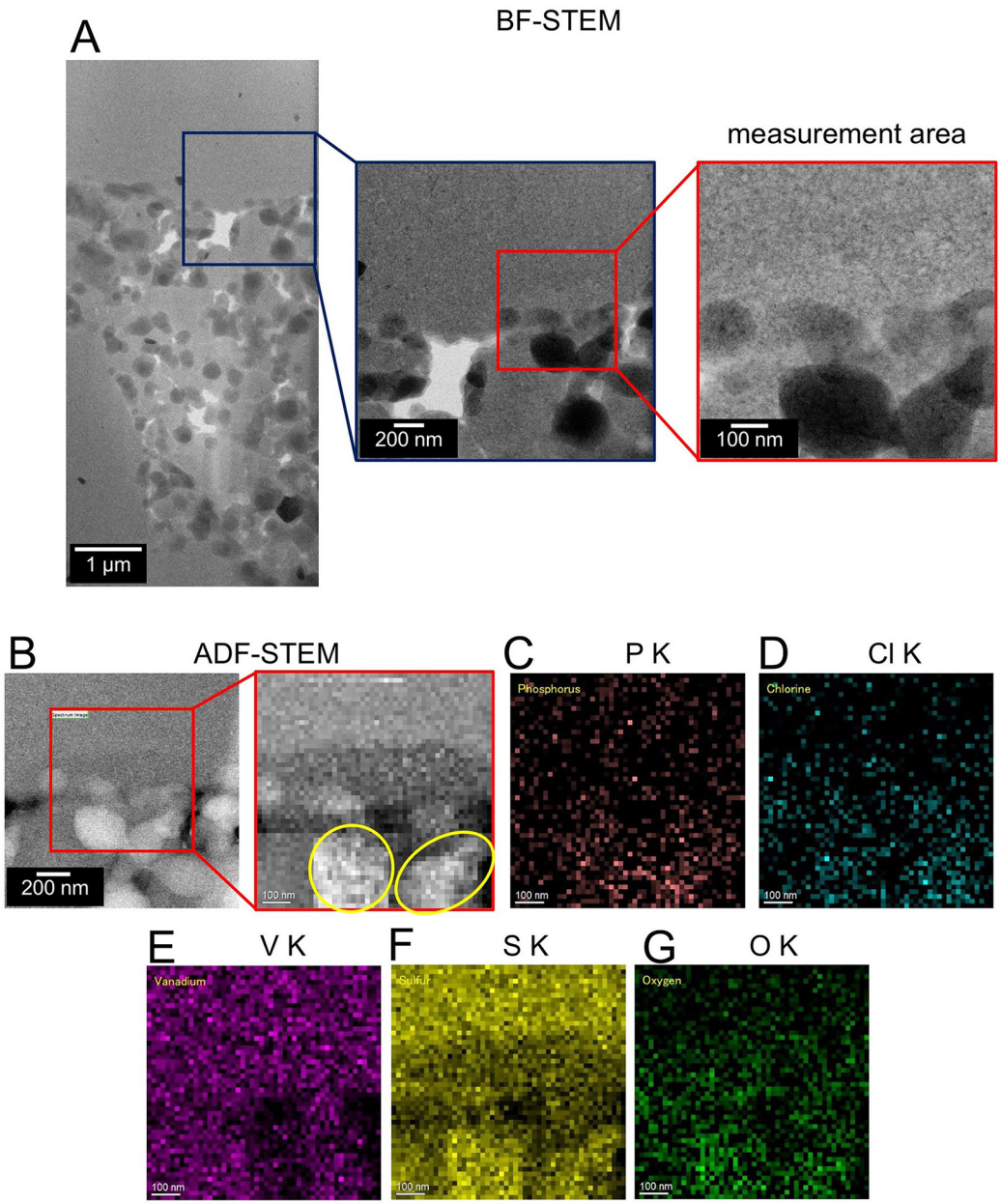

Figure 6. (A) BF-STEM images of composite cathodes consisting of $Li_8VS_{5.5}$ and the SE after the second discharge test. The EDX measurement area is highlighted by a red square. (B) ADF-STEM image and EDX mappings of (C) P, (D) Cl, (E) V, (F) S, and (G) O K-edges. Yellow circles indicate the SE areas.

Figure 7E-H shows decomposed spectra and their distribution mappings, respectively. Component 1 is distributed in the bulk of $Li_8VS_{5.5}$, whereas component 2 is observed at the interface of $Li_8VS_{5.5}$ and the SE. The V L-edge peak of component 2 is shifted to a higher position than that of component 1, indicating an increase in the valence of V. Moreover, the peak intensity of the O K-edge in component 2 is higher than that in component 1. Component 3, which shows a low intensity for the V L-edge and a high intensity for the O K-edge, is distributed mainly in the SE areas. Figure 7 indicates a deficit of Li and S and an increase in the valence of V in the $Li_8VS_{5.5}$ region near the interface of $Li_8VS_{5.5}$ and the SE, suggesting the formation of an interphase between $Li_8VS_{5.5}$ and the SE after a few charge-discharge cycles. In addition, the SE undergoes

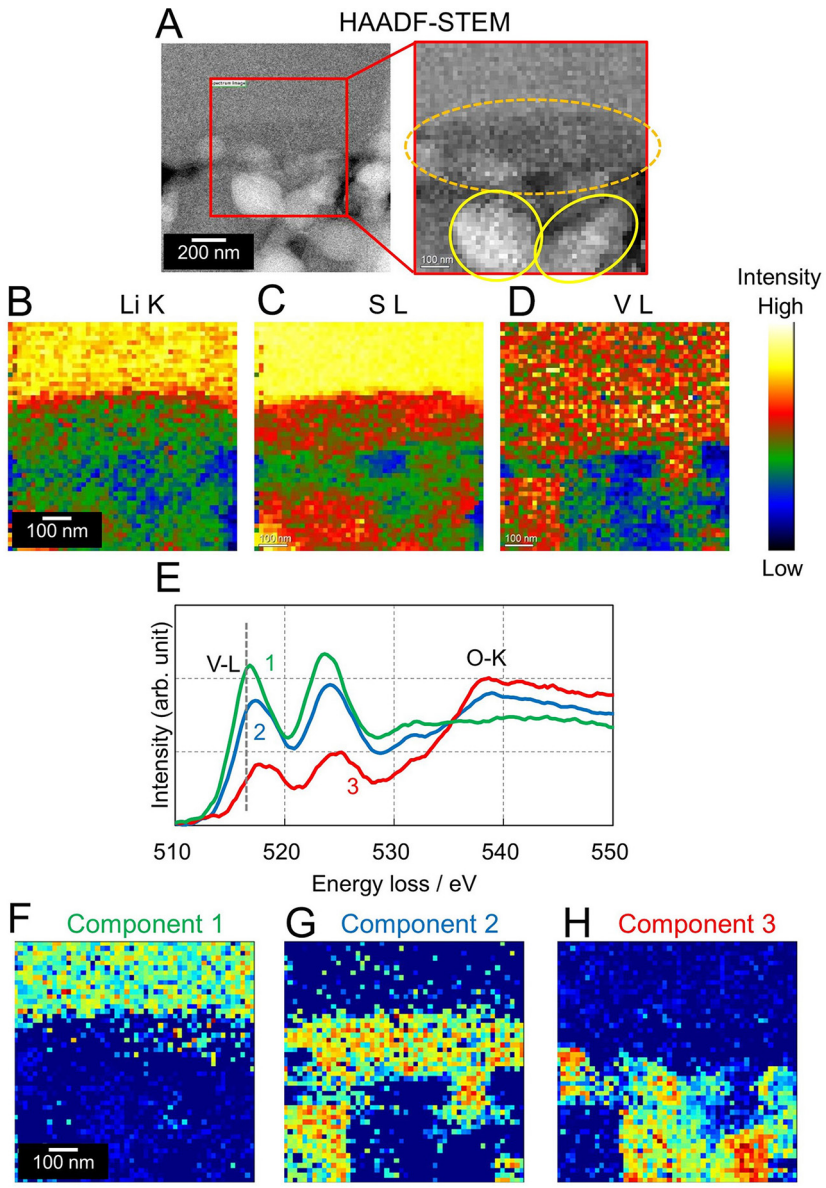

Figure 7. (A) HAADF-STEM images of composite cathodes consisting of $Li_8VS_{5.5}$ and the SE after the second discharge test. Yellow and orange dotted circles indicate the SE area and interface between $Li_8VS_{5.5}$ and the SE, respectively. STEM-EELS mappings of (B) Li, (C) S, and (D) V. (E) Sets of decomposed spectra of components 1-3 and (F-H) their distribution maps.

delithiation and partial decomposition by oxygen. Maintaining a low oxygen content can improve the cycle performance of ASSBs with Li_xVS_y. Moreover, investigating the behavior of the Li_xVS_y-SE interphase is critical for an accurate battery performance analysis.

Comparison with other lithium-containing vanadium sulfide electrodes

A comparison of $Li_8VS_{5.5}$, $90(0.75Li_2S{\cdot}0.25V_2S_3){\cdot}10LiI$[24], and core-shell $Li_2S/LiVS_2$[25] is provided in Table 2. $Li_8VS_{5.5}$ contains the highest amount of Li_2S, which is an insulator; however, because of the structure of the nanocomposite in the amorphous matrix, high electronic conductivity was obtained. Despite containing a high amount of Li_2S, ASSBs with $Li_8VS_{5.5}$ (even those with high loading) show the highest capacity among all the ASSBs with lithium-containing vanadium sulfide materials because nanosized $LiVS_2$ in the amorphous

Table 2. Comparison of the properties of $Li_8VS_{5.5}$, $90(0.75Li_2S{\cdot}0.25V_2S_3){\cdot}10LiI$, and core-shell $Li_2S/LiVS_2$

Active material	$Li_8VS_{5.5}$ (this work)	$90(0.75Li_2S{\cdot}0.25V_2S_3){\cdot}10LiI$[24]	Core shell of $Li_2S/LiVS_2$[25]
Structure	Nanocomposites of Li_2S and $LiVS_2$ in amorphous matrix	$LiVS_2$ and Li_2S-LiI nanoparticles dispersed in the Li_2S-V_2S_3-LiI amorphous matrix	Li_2S core and $LiVS_2$ shell
Feature	Sufficient electron conduction paths formed by nano $LiVS_2$, despite a high content of Li_2S	Electrode-electrolyte bifunctional material	Interfacial redox mediator (Li_xVS_2)
Synthesis	Ball milling	Ball milling	Reacting Li_2S with VCl_4 in tetrahydrofuran
Electronic conductivity at RT	0.059 S cm^{-1}	> 0.1 S cm^{-1}	5.5 S cm^{-1}
Ionic conductivity at RT	5.6×10^{-6} S cm^{-1}	2.5×10^{-4} S cm^{-1}	1.3×10^{-5} S cm^{-1}
Li_2S:$LiVS_2$	77.8:22.2 (wt.%)	50:50 (wt.%)	~60:~40 (wt.%)
Composite cathodes including active material and SE			
Active material:SE	80:20 (wt.%)	100:0 (wt.%)	50:50 (wt.%)
Li_2S in composite cathodes	62.2 wt.%	45 wt.%	~30 wt.%
Electronic conductivity at RT	1.2×10^{-2} S cm^{-1}	>0.1 S cm^{-1}	5.1×10^{-1} S cm^{-1}
Ionic conductivity at RT	2.0×10^{-5} S cm^{-1}	2.5×10^{-4} S cm^{-1}	1.5×10^{-4} S cm^{-1}
High-loading performance[a]	33 mg cm^{-2},15 mAh cm^{-2} (full cell, 60 °C, 0.2 mA cm^{-2})	*ca.* 4.5 mg cm^{-2}, *ca.* 1.7 mAh cm^{-2} (half-cell, 25 °C, 0.13 mA cm^{-2})	20 mg cm^{-2}, 5.3 mAh cm^{-2} (half-cell, 60 °C, 0.25 mA cm^{-2})

[a]The loading mass includes the active material and SE.

matrix forms sufficient electron conduction paths. Our previous study demonstrated that Li_5VS_4 and $Li_6VS_{4.5}$ exhibit superior rate performance than $Li_8VS_{5.5}$. In particular, the $Li_6VS_{4.5}$ half-cell delivered a higher areal capacity at a relatively high current density of 1.3 mA cm^{-2} compared with $90(0.75Li_2S{\cdot}0.25V_2S_3){\cdot}10LiI$[24] and core-shell $Li_2S/LiVS_2$[25] [Supplementary Table 4]. These results indicate that tuning the composition of Li_xVS_y is an effective strategy for improving rate performance.

CONCLUSIONS

Li_xVS_y synthesized by the mechanochemical treatment of Li_2S and V_2S_3 contains nanocomposites of Li_2S and $LiVS_2$ in an amorphous matrix and shows high electronic conductivity (10^{-1}-10^{-2} S cm^{-1}) and capacity (~650 mAh g^{-1}). Delithiation and lithiation proceed in both Li_2S and $LiVS_2$ during charge-discharge reactions. Moreover, $LiVS_2$ enhances the electronic conductivity of Li_xVS_y and the reversibility of charge-discharge reactions owing to its high electronic conductivity and layered structure. ASS full cells with a high mass loading of 33 and 10.4 mg cm^{-2} of a composite cathode comprising 80/20 (wt.%) of $Li_8VS_{5.5}$ and the SE and a composite Si anode, respectively, show a high areal capacity of 15 mAh cm^{-2}. According to the calculation, enlarging such full cells to

210 mm × 297 mm and stacking 20 cells results in high energy densities of 853 Wh L^{-2} and 515 Wh kg^{-1}. Notably, $Li_8VS_{5.5}$ includes the highest amount of Li_2S among the reported lithium-containing vanadium sulfide electrodes. Further studies on the volume changes of Li_xVS_y and the formation of an interphase between Li_xVS_y and the SE during charge-discharge tests could facilitate modifications that improve the cycle performance of ASSBs with Li_xVS_y. The results of this study contribute significantly toward research on ASSBs and are expected to guide future research on the design and development of high-performance ASSBs with high potential applicability in various fields.

DECLARATIONS

Authors' contributions

Made substantial contributions to the conception and design of the study and performed data analysis and interpretation: Otoyama, M.; Wanibuchi, M.
Performed data acquisition for structural characterization: Takeuchi, T.; Ishida, N.; Taguchi, N.; Kitta, M.
Supervised: Sano, H.; Kawamoto, K.; Kuratani, K.; Sakaebe, H.
All authors revised the manuscript.

Availability of data and materials

The data supporting this work is provided in the Supplementary Materials.

Financial support and sponsorship

This work was partially supported by the New Energy and Industrial Technology Development Organization (NEDO) under the SOLiD-EV Project (JPNP18003).

Conflicts of interest

All authors declared that there are no conflicts of interest.

Ethical approval and consent to participate

Not applicable.

Consent for publication

Not applicable.

REFERENCES

1. Ji, X.; Nazar, L. F. Advances in Li-S batteries. *J. Mater. Chem.* **2010**, *20*, 9821. DOI
2. Manthiram, A.; Fu, Y.; Chung, S. H.; Zu, C.; Su, Y. S. Rechargeable lithium-sulfur batteries. *Chem. Rev.* **2014**, *114*, 11751-87. DOI PubMed
3. Yamin, H.; Gorenshtein, A.; Penciner, J.; Sternberg, Y.; Peled, E. Lithium sulfur battery - oxidation reduction-mechanisms of polysulfides in Thf solutions. *J. Electrochem. Soc.* **1988**, *135*, 1045-8. DOI
4. Shim, J.; Striebel, K. A.; Cairns, E. J. The lithium/sulfur rechargeable cell: effects of electrode composition and solvent on cell performance. *J. Electrochem. Soc.* **2002**, *149*, A1321. DOI
5. Sakuda, A.; Hayashi, A.; Tatsumisago, M. Sulfide solid electrolyte with favorable mechanical property for all-solid-state lithium battery. *Sci. Rep.* **2013**, *3*, 2261. DOI PubMed PMC
6. Fujita, Y.; Münch, K.; Asakura, T.; et al. Dynamic volume change of Li_2S-based active material and the influence of stacking pressure on capacity in all-solid-state batteries. *Chem. Mater.* **2024**, *36*, 7533-40. DOI
7. Kamaya, N.; Homma, K.; Yamakawa, Y.; et al. A lithium superionic conductor. *Nat. Mater.* **2011**, *10*, 682-6. DOI
8. Kato, Y.; Hori, S.; Saito, T.; et al. High-power all-solid-state batteries using sulfide superionic conductors. *Nat. Energy.* **2016**, *1*, 201630. DOI
9. Li, Y.; Song, S.; Kim, H.; et al. A lithium superionic conductor for millimeter-thick battery electrode. *Science* **2023**, *381*, 50-3. DOI

10. Boulineau, S.; Courty, M.; Tarascon, J.; Viallet, V. Mechanochemical synthesis of Li-argyrodite Li_6PS_5X (X = Cl, Br, I) as sulfur-based solid electrolytes for all solid state batteries application. *Solid. State. Ion.* **2012**, *221*, 1-5. DOI
11. Yang, X.; Luo, J.; Sun, X. Towards high-performance solid-state Li-S batteries: from fundamental understanding to engineering design. *Chem. Soc. Rev.* **2020**, *49*, 2140-95. DOI PubMed
12. Zhang, W.; Leichtweiß, T.; Culver, S. P.; et al. The detrimental effects of carbon additives in $Li_{10}GeP_2S_{12}$-based solid-state batteries. *ACS. Appl. Mater. Interfaces.* **2017**, *9*, 35888-96. DOI
13. Strauss, F.; Stepien, D.; Maibach, J.; et al. Influence of electronically conductive additives on the cycling performance of argyrodite-based all-solid-state batteries. *RSC. Adv.* **2020**, *10*, 1114-9. DOI PubMed PMC
14. Walther, F.; Randau, S.; Schneider, Y.; et al. Influence of carbon additives on the decomposition pathways in cathodes of lithium thiophosphate-based all-solid-state batteries. *Chem. Mater.* **2020**, *32*, 6123-36. DOI
15. Fang, R.; Liu, Y.; Li, Y.; Manthiram, A.; Goodenough, J. B. Achieving stable all-solid-state lithium-metal batteries by tuning the cathode-electrolyte interface and ionic/electronic transport within the cathode. *Mater. Today.* **2023**, *64*, 52-60. DOI
16. Balach, J.; Linnemann, J.; Jaumann, T.; Giebeler, L. Metal-based nanostructured materials for advanced lithium-sulfur batteries. *J. Mater. Chem. A.* **2018**, *6*, 23127-68. DOI
17. Li, X.; Sun, X.; Xiao, B.; Wang, D.; Liang, J. Inorganic polysulfide chemistries for better energy storage systems. *Acc. Chem. Res.* **2023**, *56*, 3547-57. DOI
18. Sakuda, A. Metal polysulfides as high capacity electrode active materials - toward superior secondary batteries based on sulfur chemistry. *Electrochemistry* **2023**, *91*, 102003. DOI
19. Kawasaki, Y.; Tsukasaki, H.; Ayama, T.; et al. Synthesis and electrochemical properties of Li_3CuS_2 as a positive electrode material for all-solid-state batteries. *ACS. Appl. Energy. Mater.* **2021**, *4*, 20-4. DOI
20. Otoyama, M.; Takeuchi, T.; Taguchi, N.; Kuratani, K.; Sakaebe, H. Mechanochemical synthesis and electrochemical properties of Li_xVS_y positive electrodes for all-solid-state batteries. *ECS. Adv.* **2023**, *2*, 010501. DOI
21. Ji, Q.; Li, C.; Wang, J.; et al. Metallic vanadium disulfide nanosheets as a platform material for multifunctional electrode applications. *Nano. Lett.* **2017**, *17*, 4908-16. DOI
22. Cai, L.; Zhang, Q.; Mwizerwa, J. P.; et al. Highly crystalline layered VS_2 nanosheets for all-solid-state lithium batteries with enhanced electrochemical performances. *ACS. Appl. Mater. Interfaces.* **2018**, *10*, 10053-63. DOI
23. Xu, S.; Kwok, C. Y.; Zhou, L.; Zhang, Z.; Kochetkov, I.; Nazar, L. F. A high capacity all solid-state Li-sulfur battery enabled by conversion-intercalation hybrid cathode architecture. *Adv. Funct. Mater.* **2021**, *31*, 2004239. DOI
24. Shigedomi, T.; Fujita, Y.; Kishi, T.; et al. Li_2S-V_2S_3 -LiI bifunctional material as the positive electrode in the all-solid-state Li/S battery. *Chem. Mater.* **2022**, *34*, 9745-52. DOI
25. Kwok, C. Y.; Xu, S.; Kochetkov, I.; Zhou, L.; Nazar, L. F. High-performance all-solid-state Li_2S batteries using an interfacial redox mediator. *Energy. Environ. Sci.* **2023**, *16*, 610-8. DOI
26. Izumi, F.; Momma, K. Three-dimensional visualization in powder diffraction. *Solid. State. Phenomen.* **2007**, *130*, 15-20. DOI
27. Nakanishi, K.; Yagi, S.; Ohta, T. XAFS measurements under atmospheric pressure in the soft X-ray region. *Aip. Conf. Proc.* **2010**, *1234*, 931-4. DOI
28. Kiguchi, M.; Yokoyama, T.; Matsumura, D.; Kondoh, H.; Ohta, T.; Kitajima, Y. Interface structure of alkali-halide heteroepitaxial films studied by X-ray-absorption fine structure. *Phys. Rev. B.* **1999**, *60*, 16205-10. DOI
29. Han, F.; Yue, J.; Fan, X.; et al. High-performance all-solid-state lithium-sulfur battery enabled by a mixed-conductive Li_2S nanocomposite. *Nano. Lett.* **2016**, *16*, 4521-7. DOI
30. Gamo, H.; Hikima, K.; Matsuda, A. Understanding decomposition of electrolytes in all-solid-state lithium-sulfur batteries. *Chem. Mater.* **2022**, *34*, 10952-63. DOI
31. Kim, J. T.; Rao, A.; Nie, H. Y.; et al. Manipulating Li_2S_2/Li_2S mixed discharge products of all-solid-state lithium sulfur batteries for improved cycle life. *Nat. Commun.* **2023**, *14*, 6404. DOI PubMed PMC
32. Sun, Z.; Lai, Y.; Lv, N.; et al. Insights on the properties of the O-doped argyrodite sulfide solid electrolytes ($Li_6PS_{5-x}ClO_x$, x=0-1). *ACS. Appl. Mater. Interfaces.* **2021**, *13*, 54924-35. DOI
33. Murphy, D. W.; Cros, C.; Di Salvo, F. J.; Waszczak, J. V. Preparation and properties of LixVS2 (0 .ltoreq. x .ltoreq. 1). *Inorg. Chem.* **1977**, *16*, 3027-31. DOI